J. Fluid Mech. (1983), *vol.* 134, *pp.* 103–131
Printed in Great Britain

Flow between rotating disks. Part 1. Basic flow

By A. Z. SZERI, S. J. SCHNEIDER†, F. LABBE
Department of Mechanical Engineering, The University of Pittsburgh, Pittsburgh, PA 15261

AND H. N. KAUFMAN
Research and Development Center, Westinghouse Electric Co., Beulah Rd, Pittsburgh PA 15235

(Received 3 June 1982)

Laser-Doppler velocity measurements were obtained in water between finite rotating disks, with and without throughflow, in four cases: $\omega_1 = \omega_2 = 0$; $\omega_2/\omega_1 = -1$; $\omega_2/\omega_1 = 0$; $\omega_2/\omega_1 = 1$. The equilibrium flows are unique, and at mid-radius they show a high degree of independence from boundary conditions in r. With one disk rotating and the other stationary, this mid-radius 'limiting flow' is recognized as the Batchelor profile of infinite-disk theory. Other profiles, predicted by this theory to coexist with the Batchelor profile, were neither observed experimentally nor were they calculated numerically by the finite-disk solutions, obtained here via a Galerkin, B-spline formulation. Agreement on velocity between numerical results and experimental data is good at large values of the ratio R_Q/Re, where $R_Q = Q/2\pi\nu s$ is the throughflow Reynolds number and $R_e = R_2^2\omega/\nu$ is the rotational Reynolds number.

1. Introduction

The problem of disk flows has occupied a central position in the field of fluid mechanics in recent years. Disk flows have immediate technical applications (rotating machinery, lubrication, viscometry, heat and mass exchangers, biomechanics, oceanography), but quite apart from that they have intrinsic interest.

Relevant previous research concerned itself almost entirely with *infinite-disk flows*. The sole reason for this, one suspects, is that the similarity transformation, available when the disks are infinite, reduces the number of spatial dimensions of the problem to one. Although it is questionable whether the reduced model approximates to the physical problem of flow between finite disks, the nonlinear ordinary differential equations that define the phenomenon have been the subject of intense analytical and numerical probing. In spite of this, the nature of the basic flow is not well understood and the researchers of infinite-disk flows are responsible for one of the long-standing controversies of fluid mechanics, which concerns the uniqueness of the basic motion.

In an attempt to clarify this controversy and to establish its relevance to the physical problem we studied flows which occur between finite rotating disks. These disks may be stationary, or they may rotate in either direction. A line source or sink of variable strength is placed in coincidence with the axis of rotation. The types of instabilities that may occur in this flow, and the critical conditions for their occurrence, are discussed in the companion paper (Szeri *et al.* 1983).

A related flow, but a flow that is considerably more amenable to theoretical

† Also at Research and Development Center, Westinghouse Electric Co.

treatment than the one defined above, is due to the rotation of a *single, infinite disk*. It was first discussed by von Kármán (1921), who postulated that the axial velocity is independent of the radial coordinate. The Kármán postulate leads to a similarity transformation, which was later shown by Batchelor (1951) to be applicable even when the fluid at infinity is rotating about the axis of the disk. Solutions have been obtained for various values of γ, the ratio of angular velocity at infinity to that of the disk, by Rogers & Lance (1960) and others. However, for values of γ in the range $-0.160 > \gamma > -1.4351$ it appeared to be impossible to find solutions. It is now clear that at $\gamma = -1.4351$ the solution of the equations becomes singular. At $\gamma = -0.160$ the situation was more mysterious. Weidman & Redekopp (1975) suggested singularity in this neighbourhood. The mystery was cleared up by Zandebergen & Dijkstra (1977) and by Dijkstra (1980), who showed that branching occurs at $\gamma = -0.16054$. They discuss the two branches which coincide here, and indicate that there are an infinite number of solutions to the problem in a small region near $\gamma = 0$. Lentini & Keller (1980) find that at least four families of solutions exist and clearly indicate existence of an infinite sequence of solutions. The main difference between the solutions consists of an extra cell, which is built up as the solution proceeds from one branch into another. Near the disk and near infinity the solutions are almost indistinguishable from one another, particularly when higher branches are compared. Flows with $\gamma = 0$, having zero angular velocity at infinity, exist in each family.

Based on an examination of the governing equations, Batchelor (1951) predicted that at high Reynolds numbers a thin boundary layer will develop on each disk, with the main body of the fluid rotating at a constant rate, when the fluid is enclosed between *two infinite rotating disks*. This prediction was challenged by Stewartson (1953), who reasoned that at large Reynolds numbers the flow outside the boundary layers is purely axial.

Lance & Rogers (1961) used numerical methods to solve the two-point boundary-value problem that results from the Kárṁan similarity transformation. The solutions obtained by Lance & Rogers indicate that the small-Reynolds-number trend, on which Stewartson had based his predictions, is misleading and that Batchelor had been essentially correct when describing flow at high Reynolds numbers. Mellor, Chapple & Stokes (1968) produced several classes of solutions which are referred to as multiple-cell solutions. They gave the one-cell solution detailed treatment, and obtained experimental data for it by hot-wire anemometry on 4.29 in. radius disks separated in air by an axial distance of $\frac{1}{8}$ in. Both tangential and radial velocities were measured, and agreement between theory and data was quite good in the case of tangential velocity. However, the difference between theory and data increased near the outer radius. Comparison of the radial velocities was less satisfactory and was partly explained by the fact that the induced radial velocities were at least one order of magnitude smaller than the circumferential velocities. Also, the hot wire was calibrated in uniform flow while the measurements were made in highly sheared flow. They reasoned further that the fluid near the stationary disk was re-ingested in the apparatus and was, originally, fluid near the rotating disk. Fluid near the stationary disk had therefore higher tangential velocity at larger radii, and thus differences between theory and data were directly related to edge effects.

More recently Nguyen, Ribault & Florent (1975) found both Batchelor-type and Stewartson-type solutions numerically, with the character of the flow depending on what starting values were assumed for the marching integration. They state that: 'We cannot, of course, claim that these are the only solution, since it is impossible to try all possible initial combinations.' Holodniok, Kubicek & Hlavacek (1977)

identify as many as five solutions to the governing differential equations at a given (high) Reynolds number, two of which are of boundary-layer type. Their low-Reynolds-number solution is unique and the flow is of the Batchelor type, with a substantial portion of the fluid rotating as a rigid body. Additional solutions make their appearance as the Reynolds number is increased. Two of these solutions are of two-cell type, and there is a Stewartson-type solution exhibiting boundary layers on both disks. No physical interpretation is given to the fifth profile by Holodniok *et al.* Wilson & Schryer (1978) applied uniform suction to the rotating disk in their numerical treatment of disk flows. They find the equilibrium flow approaching the Batchelor-type flow at large Reynolds numbers, but at the same time they raise the questions as to whether other solutions to the time-dependent equations with zero initial conditions are possible. Wilson & Schryer exhibit a rotational start-up scheme, which leads to an equilibrium solution in which the interior of the fluid rotates in the direction opposing disk rotation. Holodniok, Kubicek & Hlavacek (1981) use finite-difference discretization and Newton's method to demonstrate the existence of several branches of solution. They give detailed treatment to the conditions $E^{-1} = 625$ and $\omega_1/\omega_2 = 0$, 1 and -1, where $E = \nu/s^2\omega$ is the Ekman number.

Finite disks have been studied by Szeri & Adams (1978), who used an approximation in which the radial variation of shear stress is neglected. The equations become parabolic in this approximation, and the flow is adequately described by a single dimensionless parameter, the Ekman number. An upstream initial condition is all that is required to start the solution, which is valid up to the position of incipient backflow. Various inlet flows with a given Ekman number were found to have identical dimensionless velocity profiles a short distance downstream of the inlet boundary; thus even the inlet boundary condition loses its significance. This numerical result was verified by comparison with published experimental data.

When the film between the two finite disks is 'thick', Adams & Szeri (1982) show that the flow is characterized by five dimensionless parameters and two sets of boundary conditions at the inlet and outlet radii, respectively. The five parameters are the rotational Reynolds number Re, the throughflow Reynolds number R_Q, the ratio of rotational speeds ω_2/ω_1, and two geometric ratios $\lambda = (R_2/s)^2$ and $\Delta = R_2/(R_2 - R_1)$. They use the Galerkin–Kantorovich method and circular functions to explore the effects that each of the parameters have on the flow. Their results show a recirculation cell with increasing rotational Reynolds number and suggest the formation of multiple cells at high rotational Reynolds numbers. The convergence properties of their computational scheme, however, makes this last finding suspect.

2. Test apparatus

The present study is limited to a single set of rotating disks with variable spacing. The parameter Δ is fixed and the parameter λ is limited to two values corresponding to a 'thin-film' spacing $\lambda = 6400$, and corresponding to a 'thick-film' spacing $\lambda = 406.5$ (Adams & Szeri 1982). Three angular velocity ratios ω_2/ω_1 are studied. These are: $\omega_2/\omega_1 = 0$, one disk rotating and the other stationary; $\omega_2/\omega_1 = 1$, corotating disks of equal angular velocity; and $\omega_2/\omega_1 = -1$, counter-rotating disks of equal but opposite angular velocity. In addition we investigated the condition $\omega_1 = \omega_2 = 0$. Two different sets of boundary conditions are examined for their effect on the flow. The values of Re and R_Q were chosen to explore specific flow features in each of these flows.

The test apparatus is designed so that the controlling parameters provide flows in

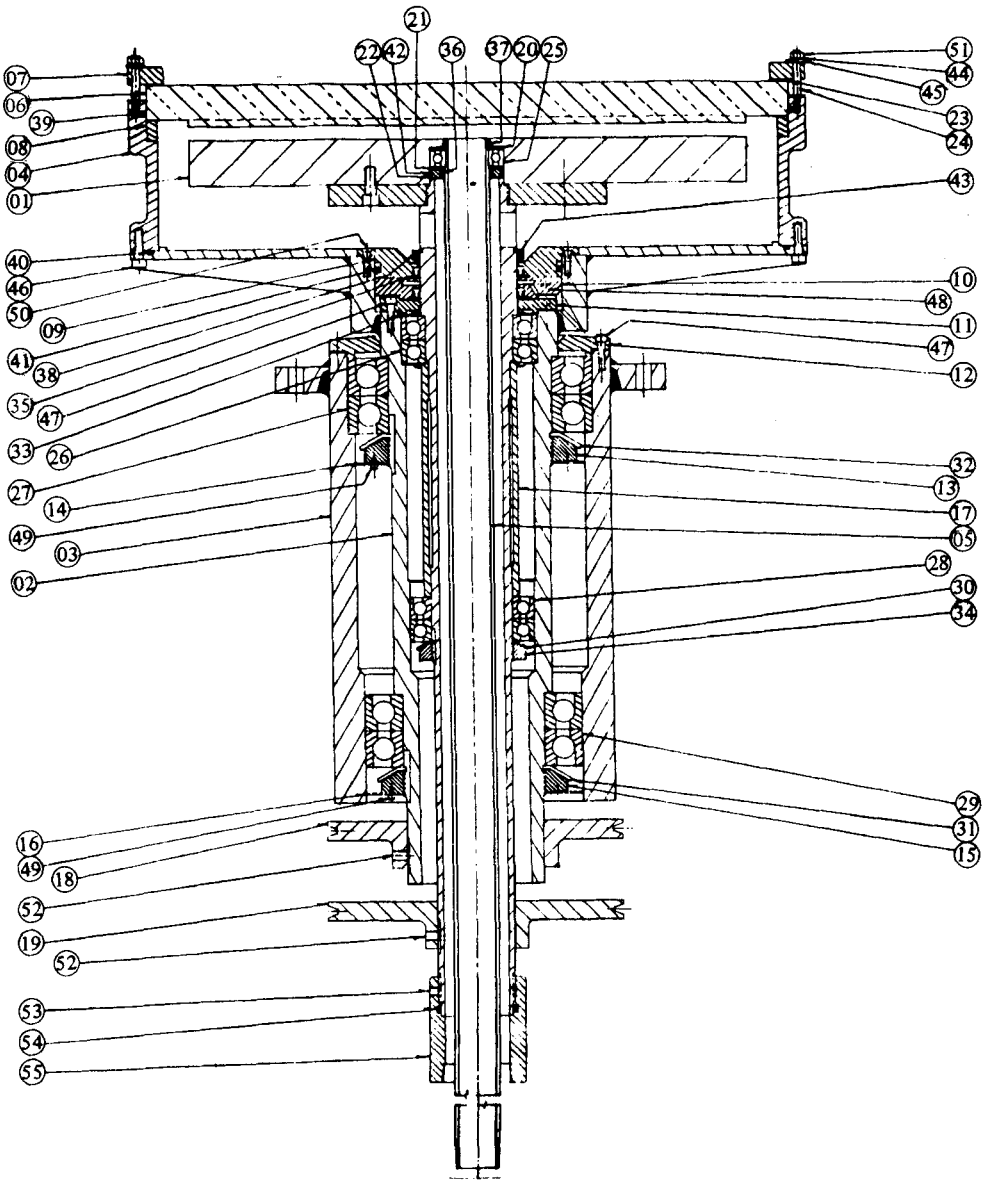

FIGURE 1. Test apparatus.

the laminar regime, through transition, and into the turbulent regime. The maximum rotational speed of the test apparatus is chosen to provide Reynolds numbers up to $Re = 3 \times 10^5$, above which Schlichting (1968) has indicated turbulence. This also provides flows well into the region of instability for single-disk flows (Gregory, Stuart & Walker 1955). In order to keep the angular velocity of the disks low, water is used as the test fluid and the disk outer radius is chosen to be $R_2 = 25.4$ cm. One then calculates rotational speed requirements of 38 rev/min for turbulence at the outer radius and 152 rev/min for turbulence at midradius. The value of the inner radius is set at $R_1 = 1.6934$ cm; thus for these experiments the parameter $\Delta = 1.0714$.

The apparatus is shown in the general assembly drawing (figure 1). It consists of

two 20 in. diameter disks, an upper glass disk and a lower metal disk, items 6 and 1 respectively in figure 1. The disks are driven by two concentric shafts. Each shaft is supported on two sets of precision duplex bearings, items 26–29, each set having a light preload. The top set of bearings of each shaft is captivated in its respective housing, items 2 and 3, and the bottom set is 'floating', thus allowing for shaft thermal expansion.

The outer housing, item 3, supports the entire assembly. The inner and outer shafts are rotated by V-belts and pulleys, items 18 and 19, to give corotation or counter-rotation relative to each other.

Water is introduced into the space between the two disks by a tube, item 5, through the centre of the inner shaft. This feed tube is supported by a ball bearing at the top, item 25, and a rotating union at the bottom. Water is fed to and drained from the apparatus through the rotating union. The feed tube is O-ring sealed to the stationary part of the union. The inner drive shaft is direct-coupled to the rotating part of the union. Water is drained from the annular space between the inside diameter of the inner drive shaft and the outside diameter of the feed tube through the rotating union.

The water is contained in the system by a housing, item 4, which surrounds the disks and also supports and seals the upper glass disk to the system. Spacing between the upper glass disk and the lower metal disk is obtained by spacer blocks, item 8, between the housing and glass disk.

Water is supplied to the feed tube by a static supply system, which is the throughflow source supply. A constant head is maintained by a make-up pump which supplies an overhead tank and an overflow pipe to maintain the fluid level. Test-fluid temperature can be controlled by coolers and heaters in the hydraulic loop. A stirrer in the overhead tank keeps particles in suspension in the test fluid for both laser velocimetry and flow-visualization tests. Flow of the test fluid is measured by bypassing the fluid into a strain-gauged weighing tank and by timing the flow.

Each disk shaft is driven by a V-belt from a 3 horsepower, 230 V, 1725 rev/min, three-phase AC induction motor. A 3:1 pulley ratio decreases the speed of the driven shafts. Each motor is controlled by an adjustable frequency motor drive using solid state circuitry. The controls provide constant torque through the test-speed range (0–500 rev/min) and allow for motor speed reversal. The motors were modified with separately driven blowers mounted on an end bell to provide cooling at low motor speeds.

Special care was taken in the selection of the materials for the disks. Several materials, including fused silica glass and acrylic plastic, were investigated for the upper disk. A borosilicate crown glass was selected because of its freedom from striae and because it contained fewer and smaller seeds (inclusions) than some of the other glasses. Glass was chosen instead of plastic because of its higher strength properties and its greater resistance to scratching. The faces of the glass disk were ground flat and parallel to better than 0.005 in. over the 20 in. diameter.

The lower disk was machined from aluminium (ASTM-B211, Alloy GS11A). This alloy has superior corrosion resistance in water and good physical properties. The surface was machined to a flatness of within 0.0005 in. and a surface finish better than 16 μin. r.m.s. Although the alloy is suitable for anodizing, the surface was left in its polished condition to have less interference with laser backscatter light and thus provide more accurate data near the disk surface.

Boundary conditions are provided by porous plastic foam with a random pore structure of 30 pores/in. These boundaries allow radial throughflow and impart a tangential velocity to the fluid equal to that of the boundary. Thus a foam insert in the stationary central tube, item 5, figure 1, imparts zero tangential velocity to

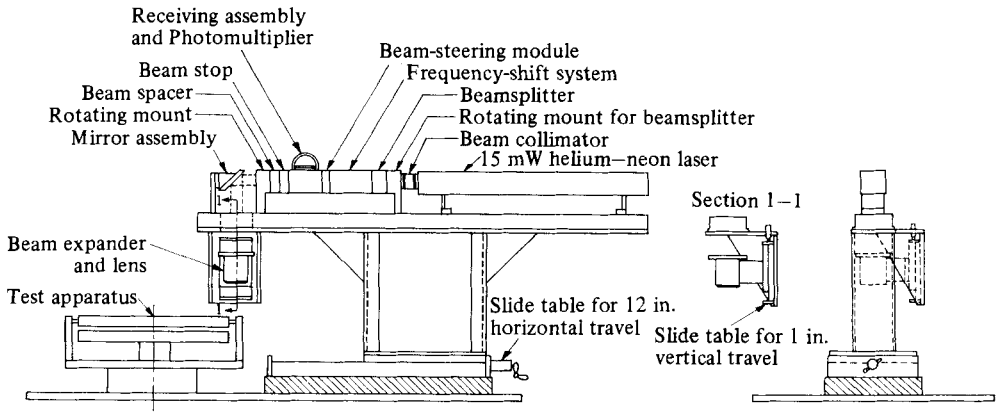

FIGURE 2. Laser-system schematics.

the fluid while an annular band of foam attached to the lower disk, item 1, figure 1, at the outer radius imparts a tangential velocity to the fluid equal to that of the bottom disk. Uniform radial flow at both the inner and outer radii is provided up to $R_Q \approx 4000$ by a pressure drop through the foam, two orders of magnitude greater than the dynamic head of the fluid.

A second boundary, referred to as the 'natural boundary', was also investigated. This is characterized by an absence of flow-straightener devices at inlet or outlet.

In order to measure the velocity of water between the disks, laser-Doppler velocimetry is used: a single-channel dual-beam system for use in the on-axis backscatter mode. The laser beam can traverse the fluid gap between the disks both radially and axially. The radial traverse is obtained by the horizontal slide with 12 in. travel. The axial or across-the-gap traverse is obtained by the vertical slide with 1 in. travel, which moves the beam expander and lens only.

Laser-Doppler velocimetry, or LDV for short, is a non-invasive optical technique which allows the measurement of the instantaneous velocity of tracer particles (1.5 μm silicon carbide, refractive index 2.65, specific gravity 3.2) suspended in the flow. This measuring technique is particularly relevant to recirculating flows. Yeh & Cummins (1964) were the first to use this technique. They eliminated the need for extensive calibration by relating signal output to particle velocity directly from physical considerations. The interference-fringe model proposed by Rudd (1969) uses constructive interference of plane waves to describe the probe volume as consisting of a set of fringe planes parallel to the bisector of the two laser beams.

The laser system used in these experiments is shown in figure 2. It is a TSI Model 9100-3, with a 45° mirror assembly for making velocity measurements in the horizontal plane of the disks. The system uses a 15 mW helium–neon laser operating in the TEM_{00} mode, which gives a continuous laser beam with a Gaussian intensity profile and a wavelength of 632.8 nm. Using $1/e^2$ of the peak intensity to define beam boundaries yields a beam diameter of 1.1 mm with a beam divergence of 1.0 mrad.

To distinguish between forward and reverse flow, an acousto-optically modulated Bragg cell is placed in the path of one of the laser beams. The Bragg cell shifts the frequency of one of the heterodyned signals relative to the other, and the photodetector gives a positive difference frequency for a stationary particle in the measuring volume. The fringe model portrays this as a moving pattern past the stationary particle. Shifting the fringes also enables the measurement of small velocities perpendicular to the fringes, when large velocities parallel to the fringes

are present. For example, when measuring small induced radial velocities, the large tangential velocities could easily sweep a particle through the probe volume without crossing enough fringes to generate an analysable signal. Shifting of the fringe pattern eliminates this deficiency.

Problems arise in the processing of the signal due to the fact that it is generated from random discrete bursts of light from individual particles. Hence special signal-processing equipment is required. Two of the types most commonly used are the frequency tracker and frequency counter, and the opportunity arose to compare these two devices. The tracker-type signal processor was used first because of its alleged ability to operate on low signal-to-noise ratios. In this instrument the Doppler difference frequency from the photomultiplier is mixed into the range of a phase-locked loop (PLL). Within its tracking range the PLL automatically adjusts the voltage of its voltage-controlled oscillator to yield the same frequency as the input signal. Thus a frequency-to-voltage conversion is effected, and an analog signal proportional to fluid velocity results. The main problem with this device is its requirement for a continuously analysable signal from the photodetector; periods of signal dropout adversely affected its operation. It was found very difficult in this system to seed the flow with just enough scattering particles for a continuous signal, without having signal interference from multiple particles in the probe volume.

The counter-type signal processor was then chosen because of its lower sensitivity to signal dropout. It measures the instantaneous velocity of individual particles by measuring the time between zero-crossings of a fixed number C of Doppler difference cycles. The time is then converted to an analog signal by a 12 bit D/A converter. The period of the C cycles is measured to 2 ns resolution. This allows excellent timing accuracy even at the highest anticipated velocities. For example, if the time to cross $C = 8$ fringes is measured on a particle moving at 1.4 m/s the time is 0.715 ± 0.002 μs, yielding a timing accuracy of 0.02 %. Other timing errors could result when noise on the signal causes false zero-crossings and miscounts of the number of cycles. This inaccuracy in the data is reduced by data validation circuitry which measures the time both for C and for $\frac{1}{2}C$ cycles. The time intervals per cycle must agree one with another within a selected percentage, usually 1 %, or the data point is rejected.

The analog signal from the counter is processed by a Norland 3001 Processing Digital Oscilloscope. The instrument performs statistical analysis on the data and registers the mean value and the standard deviation and has the capability of going from the time domain into the frequency domain. The mean value, considered to be a single measurement, represents 1024 to 4096 data points taken at equal time intervals, usually 50–100 ms in steady laminar flow.

3. Mathematical model

For rotationally symmetric flows in polar coordinates the Navier–Stokes equations are

$$\frac{\partial V_r}{\partial t} + V_r \frac{\partial V_r}{\partial r} - \frac{V_\theta^2}{r} + V_z \frac{\partial V_r}{\partial z} = \nu\left(\nabla^2 V_r - \frac{V_r}{r^2}\right) - \frac{1}{\rho}\frac{\partial p}{\partial r}, \tag{1a}$$

$$\frac{\partial V_\theta}{\partial t} + \frac{V_r}{r}\frac{\partial}{\partial r}(rV_\theta) + V_z \frac{\partial V_\theta}{\partial z} = \nu\left(\nabla^2 V_\theta - \frac{V_\theta}{r^2}\right), \tag{1b}$$

$$\frac{\partial V_z}{\partial t} + V_r \frac{\partial V_z}{\partial r} + V_z \frac{\partial V_z}{\partial z} = \nu \nabla^2 V_z - \frac{1}{\rho}\frac{\partial p}{\partial z} \quad (0 < R_1 < r < R_2;\ 0 < z < s). \tag{1c}$$

The pertinent form of the equation of continuity

$$\frac{\partial}{\partial r}(rV_r)+\frac{\partial}{\partial z}(rV_z)=0 \tag{2}$$

is identically satisfied by taking

$$V_r=\frac{1}{r}\frac{\partial\psi}{\partial z},\quad V_z=-\frac{1}{r}\frac{\partial\psi}{\partial r}. \tag{3}$$

Further simplification results when the pressure is eliminated between (1*a*) and (1*b*) by cross-differentiation.

The strategy is solution of the time-dependent problem (1), (2) by the Galerkin method with B-spline spatial discretization. Steady state is obtained as the stationary solution of the unsteady problem. If non-dimensional variables are chosen according to

$$\bar{z}=\frac{z}{s},\quad \bar{r}=\frac{r-R_1}{R_2-R_1},\quad \bar{t}=\omega t,$$

$$\psi=\frac{\psi}{sR_2^2\omega},\quad X(\bar{r})\,\Omega=\frac{V_\theta}{R_2\omega} \tag{4}$$

the system of equations (1) and (2) reduces to

$$\frac{\partial(X\mathrm{D}^2\psi)}{\partial t}+\Delta\frac{\partial\psi}{\partial z}\frac{\partial(\mathrm{D}^2\psi)}{\partial r}-\Delta\frac{\partial\psi}{\partial r}\frac{\partial(\mathrm{D}^2\psi)}{\partial z}-\lambda\frac{\partial(X\Omega^2)}{\partial z}=\frac{1}{Re}\left(X^3\mathrm{D}^2+4\Delta\frac{\partial}{\partial r}\right)\mathrm{D}^2\psi, \tag{5a}$$

$$\frac{\rho^2\partial(X\Omega)}{\partial t}+\Delta\frac{\partial\psi}{\partial z}\frac{\partial(X^2\Omega)}{\partial r}-\Delta\frac{\partial\psi}{\partial r}\frac{\partial(X^2\Omega)}{\partial z}=\frac{1}{Re}X^3\mathrm{D}^2(X^2\Omega) \tag{5b}$$

over the unit square

$$R=\{(r,z)\colon 0<r<1,0<z<1\}.$$

In this formulation $\omega=\omega_1$, unless $\omega_1=0$, in which case $\omega=\omega_2$. We have also made use of the notation

$$\lambda=\left(\frac{R_2}{s}\right)^2,\quad \Delta=\frac{R_2}{R_2-R_1},\quad X(\bar{r})=\frac{\bar{r}}{\Delta}+\frac{R_1}{R_2}, \tag{6}$$

and dropped the bar that signified dimensionless variables in (4) and (6). The operator D^2 is defined by

$$\mathrm{D}^2=\frac{1}{r^2}\left(\Delta^2\frac{\partial^2}{\partial r^2}-\frac{\Delta}{r}\frac{\partial}{\partial r}+\lambda\frac{\partial^2}{\partial z^2}\right).$$

The boundary conditions of the problem are given in non-dimensional form by

$$\frac{\partial\psi}{\partial z}=\psi=0,\quad \Omega=\frac{\omega_1}{\omega}\quad (z=0), \tag{7a}$$

$$\frac{\partial\psi}{\partial z}=0,\quad \psi=\frac{R_Q}{Re},\quad \Omega=\frac{\omega_2}{\omega}\quad (z=1), \tag{7b}$$

$$\psi=\phi^{(1)},\quad \frac{\partial\psi}{\partial r}=\Delta\phi_*^{(1)},\quad \Omega=\theta^{(1)}\quad (r=0), \tag{7c}$$

$$\psi=\phi^{(2)},\quad \frac{\partial\psi}{\partial r}=\Delta\phi_*^{(2)},\quad \Omega=\theta^{(2)}\quad (r=1), \tag{7d}$$

where $\phi^{(i)},\phi_*^{(i)},\theta^{(i)},i=1,2$, are assigned functions of z.

Let $\{A_i(r)\colon 1 \leqslant i \leqslant N_r\}$ be the set of normalized B-splines relative to k_r, π_r, ν_r; and let $\{B_j(z)\colon 1 \leqslant j \leqslant N_z\}$ be the set of normalized B-splines relative to k_z, π_z, ν_z (deBoor 1978). Here k, π and ν represent the order of the splines, the partition and the smoothness index respectively. We seek approximate solutions to (5a, b) in the form

$$\begin{aligned}\theta(r,z,t) &= \sum_{i=1}^{N_r}\sum_{j=1}^{N_z}\theta_{ij}(t)\,A_i(r)\,B_j(z)\\ &= \sum_{\hat{n}_r<i<\hat{N}_r}\ \sum_{\hat{n}_z<j<\hat{N}_z}\theta_{ij}(t)\,A_i(r)\,B_j(z)\\ &\quad+\sum_{j=1}^{N_z}\Big[\sum_{i=1}^{\hat{n}_r}\theta_{ij}(t)A_i(r)\,B_j(z)+\sum_{j=\hat{N}_r}^{N_r}\theta_{ij}(t)\,A_i(r)\,B_j(z)\Big]\\ &\quad+\sum_{\hat{n}_r<i<\hat{N}_r}\Big[\sum_{j=1}^{\hat{n}_z}\theta_{ij}(t)\,A_i(r)\,B_j(z)+\sum_{j=\hat{N}_z}^{N_z}\theta_{ij}(t)\,A_i(r)\,B_j(z)\Big].\end{aligned}\tag{8}$$

In the second expression we have grouped the set τ_0 that is associated with the essential boundary conditions.

The set

$$\tau^{\mathrm{T}} = \{A_i(r)\,B_j(z)\colon \hat{n}_r \leqslant i \leqslant \hat{N}_r, \hat{n}_z \leqslant j \leqslant \hat{N}_z\},$$

which vanishes on ∂R_0, viz that part of the boundary ∂R for which the boundary conditions are essential, will provide a basis for functions defined on the region R.

The set

$$\tau_0 = \{A_1(r)\,B_j(z), A_i(r)\,B_1(z), A_{N_r}(r)\,B_j(z), A_i(r)\,B_{N_z}(z)\colon \hat{n}_r \leqslant i \leqslant \hat{N}_r, 1 \leqslant j \leqslant N_z\}$$

when restricted to ∂R_0 provides a basis for functions defined on ∂R_0.

In an application of Galerkin's method, expansions of type (8)

$$\psi(r,z,t) = \sum_{i=1}^{N_r}\sum_{j=1}^{N_z}\psi_{ij}(t)\,A_i(r)\,B_j(z),\tag{9a}$$

$$\Omega(r,z,t) = \sum_{i=1}^{N_r}\sum_{j=1}^{N_z}\Omega_{ij}(t)\,A_i(r)\,B_j(z)\tag{9b}$$

are substituted into (5a, b). The first of the resulting equations is multiplied through by elements of the test set τ^{ψ} and the second equation by elements of τ^{Ω}:

$$\tau^{\psi} = \{A_i(r)\,B_j(z)\colon 3 \leqslant i \leqslant N_r-2, 3 \leqslant j \leqslant N_z-2\},\tag{10a}$$

$$\tau^{\Omega} = \{A_i(r)\,B_j(z)\colon 2 \leqslant i \leqslant N_r-1, 2 \leqslant j \leqslant N_z-1\}.\tag{10b}$$

This application of Galerkin's method leads to the following two sets of ordinary differential equations:

$$\begin{aligned}&\sum_{i=1}^{N_r}\sum_{j=1}^{N_z}\frac{\mathrm{d}\psi_{ij}}{\mathrm{d}t}\,[\overline{\mathbf{z}}_{lj}^{(0)}\,(\Delta^2\,\overline{\boldsymbol{p0}}_{ki}^{(2)}-\Delta\,\overline{\boldsymbol{n1}}_{ki}^{(1)})+\overline{\lambda\mathbf{z}}_{lj}^{(2)}\,\overline{\boldsymbol{p0}}_{ki}^{(0)}]\\ &=\sum_{i,\,p=1}^{N_r}\sum_{j,\,t=1}^{N_z}[\psi_{ij}\psi_{pt}\{\overline{\boldsymbol{Z}}_{ltj}^{(1)}\,[\Delta^3\,(\overline{\boldsymbol{N1}}_{kip}^{(4)}+\overline{\boldsymbol{N1}}_{ikp}^{(4)})\\ &\quad+\Delta^2\,(2\,\overline{\boldsymbol{N2}}_{kip}^{(2)}-\overline{\boldsymbol{N2}}_{kip}^{(3)}-\overline{\boldsymbol{N2}}_{ikp}^{(3)})-3\Delta\,\overline{\boldsymbol{N3}}_{kip}^{(1)}]\\ &\quad+\lambda\,\overline{\boldsymbol{Z}}_{ljt}^{(4)}\,[\Delta\,(\overline{\boldsymbol{N1}}_{kpi}^{(1)}+\overline{\boldsymbol{N1}}_{ipk}^{(1)}+2\,\overline{\boldsymbol{N2}}_{kip}^{(0)}\\ &\quad-\Delta^2\,(\Delta\overline{\boldsymbol{N1}}_{kip}^{(4)}-\overline{\boldsymbol{N2}}_{kip}^{(3)})\,(\overline{\boldsymbol{Z}}_{ltj}^{(1)}+\overline{\boldsymbol{Z}}_{jtl}^{(1)})-\lambda\Delta\,\overline{\boldsymbol{N1}}_{kpi}^{(1)}\,(\overline{\boldsymbol{Z}}_{ljt}^{(4)}+\overline{\boldsymbol{Z}}_{jtl}^{(4)})\}\\ &\quad+2\lambda\,\overline{\boldsymbol{P2}}_{kpi}^{(0)}\,\overline{\boldsymbol{Z}}_{ljt}^{(1)}\,\Omega_{ij}\Omega_{pt}]\end{aligned}$$

$$+\frac{1}{Re}\sum_{i=1}^{N_r}\sum_{j=1}^{N_z}\psi_{ij}\{\bar{z}_{lj}^{(0)}[\Delta^4\overline{p0}_{ik}^{(5)}+2\Delta^3\overline{n1}_{ki}^{(4)}+\Delta^2\overline{n2}_{ki}^{(2)}-3\Delta\overline{n3}_{ki}^{(1)}]$$

$$+\lambda\bar{z}_{lj}^{(2)}(2\Delta^2\overline{p0}_{ki}^{(2)}-2\Delta\overline{n1}_{ki}^{(1)})+\lambda^2\overline{p0}_{ki}^{(0)}\bar{z}_{lj}^{(5)}\}$$

$$(3\leqslant k\leqslant N_r-2;\ 3\leqslant l\leqslant N_z-2), \quad (11a)$$

$$\sum_{i=1}^{N_r}\sum_{j=1}^{N_z}\frac{d\Omega_{ij}}{dt}\overline{p4}_{ki}^{(0)}\bar{z}_{lj}^{(0)}=\sum_{i,\,p=1}^{N_r}\sum_{j,\,t=1}^{N_z}\psi_{ij}\Omega_{pt}\{\overline{Z}_{tj}^{(1)}[\Delta\overline{P3}_{kip}^{(1)}+2\overline{P2}_{kpi}^{(0)}]-\Delta\overline{P3}_{kpi}^{(1)}\overline{Z}_{tjl}^{(1)})\}$$

$$+\frac{1}{Re}\sum_{i=1}^{N_r}\sum_{j=1}^{N_z}\Omega_{ij}[\bar{z}_{lj}^{(0)}(3\Delta\overline{p3}_{ki}^{(1)}+\Delta^2\overline{p4}_{ki}^{(2)})+\lambda\bar{z}_{lj}^{(2)}\overline{p4}_{ki}^{(0)}]$$

$$(2\leqslant k\leqslant N_r-1;\ 2\leqslant l\leqslant N_z-1). \quad (11b)$$

The Galerkin coefficients $\bar{z}_{ij}^{(0)}$, $\overline{p0}_{ki}^{(2)}$, ... are defined in the appendix.

The boundary conditions at $z=0,1$ are easiest to satisfy in the strong form. The condition $\psi=R_Q/Re$ at $z=1$, for example, can be written as

$$\sum_{i=1}^{N_r}\psi_{i,N_z}B_i(r)=\frac{R_Q}{Re}$$

or as

$$\sum_{i=1}^{N_r}\left(\psi_{i,N_z}-\frac{R_Q}{Re}\right)B_i(r)=0$$

on account of certain properties of normalized B-splines. And as the $B_i(r)$ are linearly independent, this leads to

$$\psi_{i,N_z}=\frac{R_Q}{Re}.$$

The coefficients determined in this manner are

$$\psi_{i,1}=\psi_{i,2}=0,\quad \psi_{i,N_z}=\psi_{i,N_z-1}=\frac{R_Q}{Re},\quad \Omega_{i,1}=\frac{\omega_1}{\omega},\quad \Omega_{i,N_z}=\frac{\omega_2}{\omega}, \quad (12)$$

The boundary conditions at $r=0,1$ are satisfied in the weak form, leading the direct evaluation of the following coefficients:

$$\sum_{j=3}^{N_z-2}\bar{z}_{kj}^{(0)}\psi_{1,j}\overline{BC1}_k^{(1)},\quad \sum_{j=3}^{N_z-2}\bar{z}_{kj}^{(0)}\psi_{2,j}=\overline{BC1}_k^{(1)}-\overline{BC1}_k^{(2)}, \quad (13a,b)$$

$$\sum_{n=2}^{N_z-1}\bar{z}_{mn}^{(0)}\Omega_{1,n}=\overline{BC1}_m^{(3)},\quad \sum_{j=3}^{N_z-2}\bar{z}_{kj}^{(0)}\psi_{N_r,j}=\overline{BC2}_k^{(1)}, \quad (13c,d)$$

$$\sum_{j=3}^{N_z-2}\bar{z}_{kj}^{(0)}\psi_{N_r-1,j}=\overline{BC2}_k^{(1)}-\overline{BC2}_k^{(2)},\quad \sum_{n=2}^{N_z-1}\bar{z}_{mn}^{(0)}\Omega_{N_r,n}=\overline{BC2}_m^{(3)}$$

$$(2\leqslant m\leqslant N_z-1;\ 3\leqslant k\leqslant N_z-2). \quad (13e,f)$$

The boundary coefficients $\overline{BC1}_k^{(1)}$, $\overline{BC1}_k^{(2)}$,...of the above equations are defined in the appendix. The formulation allows for arbitrary positioning of the breakpoints and for splines of arbitrary order.

Galerkin's method permits solution of the problem not only in its unsteady form (1) but also in its steady form. We had good experiences with this method when treating the steady-state version of (1), using circular functions as test functions (Adams & Szeri 1982). The present analysis employs B-spline test functions. They

are attractive to use here as the boundary conditions are simple. Furthermore, (i) B-splines have good approximating properties, with an error term that is inversely proportioned to $(N-1)^4$ (Hall 1968), (ii) they have local support so that the storage requirement of an m-dimensional Galerkin coefficient in the, say, r-direction is $N_r \times (k_r-1)^m$ and (iii) they are easy to use when utilizing the subroutine package of deBoor (1978).

Thin-film approximation

Considerable simplification of these equations can be achieved when $s/R \ll 1, R_Q \gg 1$. The equation of continuity is satisfied by taking (Szeri & Adams 1978)

$$V_r = \frac{\nu R_Q^{\frac{1}{2}}}{s\rho}\frac{\partial\psi}{\partial z}, \quad V_\theta = s R_Q^{\frac{1}{2}}\omega\rho\Omega, \quad V_z = -\frac{\nu}{s\rho}\frac{\partial\psi}{\partial\rho}. \tag{14}$$

For this case we have $\mathrm{D}^2 = (R_Q\partial^2/\partial z^2)/\rho^2$, and (5$a$, b) reduce to

$$\frac{\partial\psi}{\partial z}\frac{\partial}{\partial\rho}\left(\frac{1}{\rho^2}\frac{\partial^2\psi}{\partial z^2}\right) - \frac{\partial\psi}{\partial\rho}\frac{\partial}{\partial z}\left(\frac{1}{\rho^2}\frac{\partial^2\psi}{\partial z^2}\right) - \frac{2}{E^2}\Omega\frac{\partial(\rho\Omega)}{\partial z} = \frac{1}{\rho}\frac{\partial^2\psi}{\partial z^4}, \tag{15a}$$

$$\frac{\partial\psi}{\partial z}\frac{\partial(\rho^2\Omega)}{\partial\rho} - \frac{\partial\psi}{\partial\rho}\frac{\partial(\rho^2\Omega)}{\partial z} = \rho\frac{\partial^2(\rho^2\Omega)}{\partial z^2}. \tag{15b}$$

$\rho = r/s R_Q^{\frac{1}{2}}$ and z are dimensionless coordinates in the radial direction and normal to the disks respectively.

This model ignores radial variations of shear stress in the steady-state equations; the resulting system remains of second order in the axial direction, but only of first order in the radial coordinate. It is an initial boundary-value problem, and is somewhat analogous to the full, time-dependent problem of the basic flow. We have implemented two different schemes for the solution of the simplified problem.

(*a*) In the first instance we seek representations of the stream function $\psi(r,z)$ and the angular-velocity function $\Omega(r,z)$ in terms of B-splines as

$$\psi(r,z) = \sum_{i=1}^{N}\psi_i(r)\,B_i(z), \quad \Omega(r,z) = \sum_{i=1}^{N}\Omega_i(r)\,B_i(z). \tag{16a, b}$$

In this formulation the boundary conditions occur as algebraic constraints; they are simplest to satisfy in the strong form. This leads to

$$\psi_1 = \psi_2 = \Omega_1 = 0, \quad \psi_{N-1} = \psi_N = \Omega_N = 1. \tag{17}$$

The system of $2N-6$ differential equations in $2N-6$ dependent variables $\psi_i, 3 \leqslant i \leqslant N-2$; $\Omega_j, 2 \leqslant j \leqslant N-1$ is as follows:

$$\sum_{j,k=1}^{N}(\bar{Z}^{(4)}_{ikj} + \bar{Z}^{(4)}_{jik} + \bar{Z}^{(4)}_{ijk})\,\psi'_j\psi_k$$
$$= \frac{2}{\rho}\sum_{j,k=1}^{N}\bar{Z}^{(4)}_{ikj}\,\psi_j\psi_k - \rho\frac{r^3}{E^2}\sum_{j,k=1}^{N}\bar{Z}^{(1)}_{ikj}\,\Omega_k\Omega_j + \rho\sum_{j=1}^{N}\bar{z}^{(5)}_{ij}\,\psi_j \quad (3 \leqslant i \leqslant N-2), \tag{18a}$$

$$-\sum_{j,k=1}^{N}\bar{Z}^{(1)}_{mjk}\,\Omega_k\psi'_j + \sum_{j,k=1}^{N}\bar{Z}^{(1)}_{mkj}\,\Omega_k\psi_j$$
$$= -\frac{2}{\rho}\sum_{j,k=1}^{N}\bar{Z}^{(1)}_{mkj}\,\Omega_k\psi_j + \rho\sum_{j=1}^{N}\bar{z}^{(2)}_{mj}\,\Omega_j \quad (2 \leqslant m \leqslant N-1). \tag{18b}$$

(*b*) In the second instance we perturb the creeping flow $\{\psi_0, \Omega_0\}$ and seek representation in the form

$$\psi(r,z) = \psi_0(z) + \sum_{i=1}^{N_\psi} \psi_i(r)\, A_i(z), \tag{19a}$$

$$\Omega(r,z) = \Omega_0(z) + \sum_{i=1}^{N_\Omega} \Omega_i(r)\, C_i(z). \tag{19b}$$

Here the spline bases $\{A_i\}_1^{N_\psi}, \{C_i\}_1^{N_\Omega}$ are so constructed by judicious placing of the breakpoints that each member of the two series vanishes, together with the required number of their derivatives, on the boundaries. The boundary conditions are then satisfied by the creeping-flow solution. For details the reader may consult Labbe (1981).

Each of the 'thin-film' formulations allows for arbitrary number and positioning of breakpoints and for arbitrary order of splines.

4. Results and discussion

The spread of data of steady-flow velocity measurements can be characterized by a standard deviation of $\sigma = 0.05$ cm/s. Approximately half of the spread is attributable to inaccuracies in electronic signal processing. The remainder is due to the fringes in the probe volume not being parallel and to the presence of velocity gradients in the probe volume.

The probe reference positions $(R_1, 0)$ and (R_1, s) were found by observing light scattering from the surfaces of the disks. Owing to the fact that the three media that the laser beams travel through, viz air, glass and water, differ from one another optically, s_w, the vertical slide travel when moving the probe volume from disk to disk, is not equal to the disk spacing s. The two distances are related by the formula $s_w = 0.7524s$. Measured and calculated values of s_w were found to agree with one another within one half of probe volume length, i.e. within ± 0.01 cm. Relative positioning of the probe volume is estimated to be accurate within ± 0.0018 cm axially and ± 0.0012 cm radially. In order to gain confidence with the LDV system, an aerosol generator was used to atomize water. A steady flow was then established inside a 1.27 cm diameter Plexiglas tube and the droplet generation rate was adjusted until a relatively continuous series of Doppler-burst signals was observed on the oscilloscope. Velocity profile was then measured in the 'fully developed' flow region of the tube, using both a tracker and a counter-type signal processor. Agreement between the two processors was better than $\pm 1\,\%$ at all radial positions, and agreement between measurement and the theoretical profile was better than $\pm 2\,\%$ (Schneider 1982).

Stationary disks ($\omega_1 = \omega_2 = 0$)

Two sets of data of the non-dimensional radial velocity $\bar{\bar{V}}_r$, where $\bar{\bar{V}}_r = sV_r/\nu R_Q^1$, are shown in figures 3 and 4, both obtained between stationary disks with a disk separation of $s = 0.3175$ cm. We were able to approach the disks within $z/s = 0.02$, i.e within 0.0064 cm. The flow was a relaminarized flow in both cases (Kreith 1965). Flow separation at the walls was not evident, possibly owing to a favourable pressure gradient caused by relaminarization. In fact, we were unable to show experimentally flow separation at the walls under any conditions, in contradiction to theory (Adams & Szeri 1982).

Although it is not possible to set $E^{-1} = 0$ in the 'thin-film' model to simulate

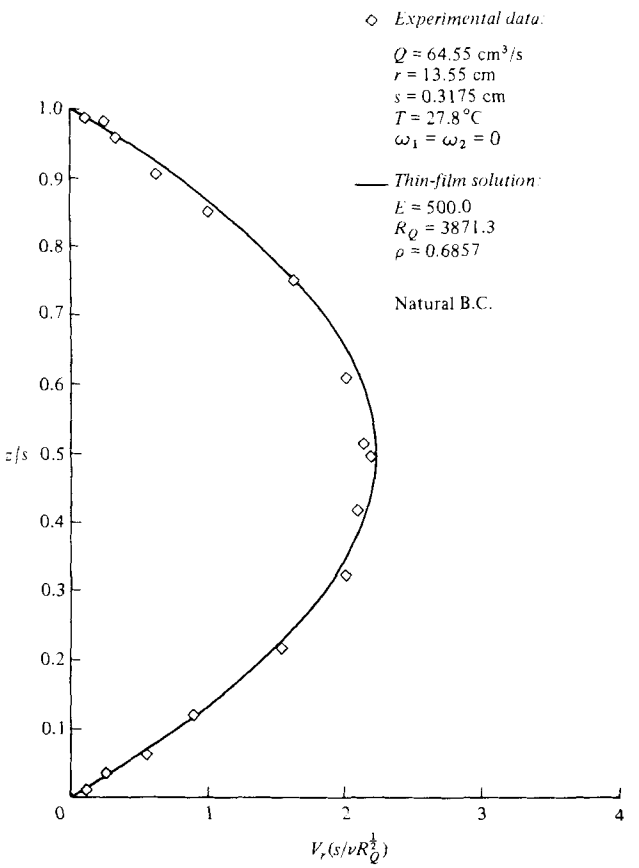

FIGURE 3. Radial velocity, stationary disks.

stationary disks, large values of the Ekman number will approximate to this condition. The thin-film solutions displayed in figures 3 and 4 were obtained with $E = 500$, giving Rossby numbers $Ro = 1.062 \times 10^3$ and 1.04×10^3 respectively. The figures cannot differentiate between the two thin-film schemes, the algebraic constraints scheme and the perturbation scheme. Figure 4 also displays the corresponding stationary solution of the full equations, demonstrating that the latter and the thin-film models are identical under proper conditions. Agreement between theory and experiment is very satisfactory for flow between stationary disks. This lends confidence not only to the LDV measurements but also to the theory, at least at large values of the Rossby number.

One disk rotating ($\omega_2/\omega_1 = 0$)

Figure 5 shows experimental data taken at $r = 19.46$ cm, with $Q = 92.1$ cm³/s and $N_1 = 2.907$ rev/min. The scatter of experimental data is more pronounced than with both disks stationary. The flow is a radial outflow everywhere in the channel, but the profile is no longer symmetric to midchannel, as the centrifugal force field is causing the fluid to increase its radial outward velocity near the rotating disk. The return flow, which is to compensate for centrifugal effects and is located near the stationary disk, is not sufficient to overcome the source flow. As backflow is not encountered for $\rho \leqslant 0.8159$, where equality specifies the non-dimensional radial

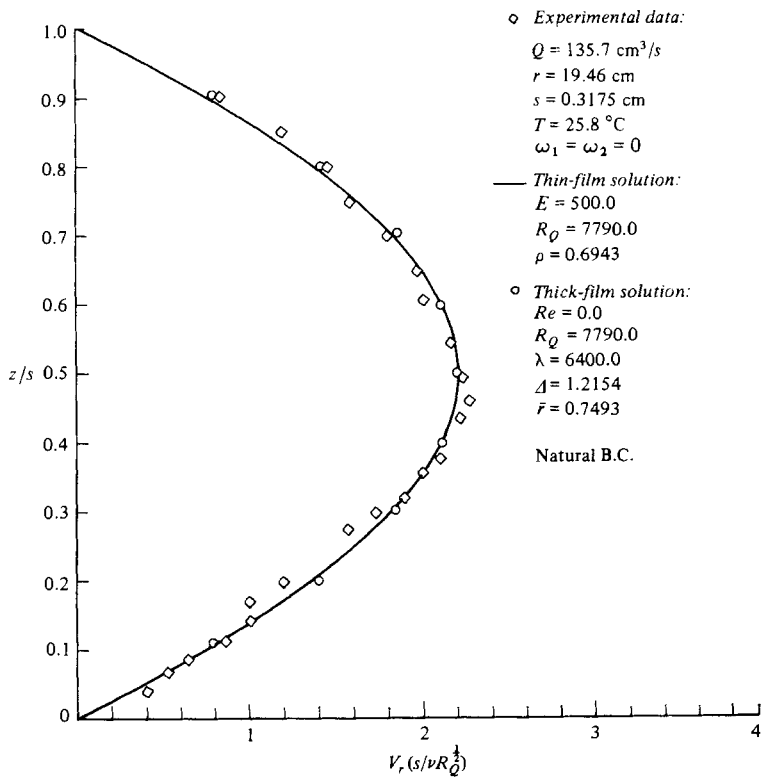

FIGURE 4. Radial velocity, stationary disks.

position at which the profile was obtained, the thin-film approximation remains applicable. Figure 5 contains the solution of the thin-film model as well as the stationary solution of the full equations. Scatter of the experimental data is too large to permit conclusions as to the accuracy of the 'thin-film' approximation versus the stationary solution of the full equations. Based on convergence studies, such as shown in tables 1 and 3 for radial velocity and in tables 2 and 4 for tangential velocity, we conclude, however, that, when it is applicable, the thin-film solution yields accurate results.

The results displayed in figure 5 should not be interpreted as indicating the inapplicability of the thin-film model under the conditions of the experiments. Rather, they demonstrate an inadequacy of resolution of the stationary solution. In fact, this is the first indication of a problem encountered progressively as $R_Q/Re \to 0$. Figure 6 shows higher rotation $N_1 = 36.38$ rev/min and a smaller throughflow $Q = 16.51$ cm³/s. The theoretical value of the non-dimensional velocity $\bar{V}_r$, where $\bar{V}_r = V_r/R_2\omega$, still follows the data points, but the agreement is less impressive. Centrifugal effects are strong enough under these conditions to create a single toroidal cell. Upon decreasing the through-flow to zero, agreement between theory and experiment becomes even less satisfactory, as shown in figure 7. In fact theory predicts the formulation of a second, corotating cell. This can be seen in figure 8, which shows contour plots of streamlines and vorticity lines.

We have been unable to identify a second cell experimentally, except when it was created by inlet flow lip separation, as shown in figure 9. The 'natural boundary conditions' of the experiments reported in this figure signify the boundary conditions

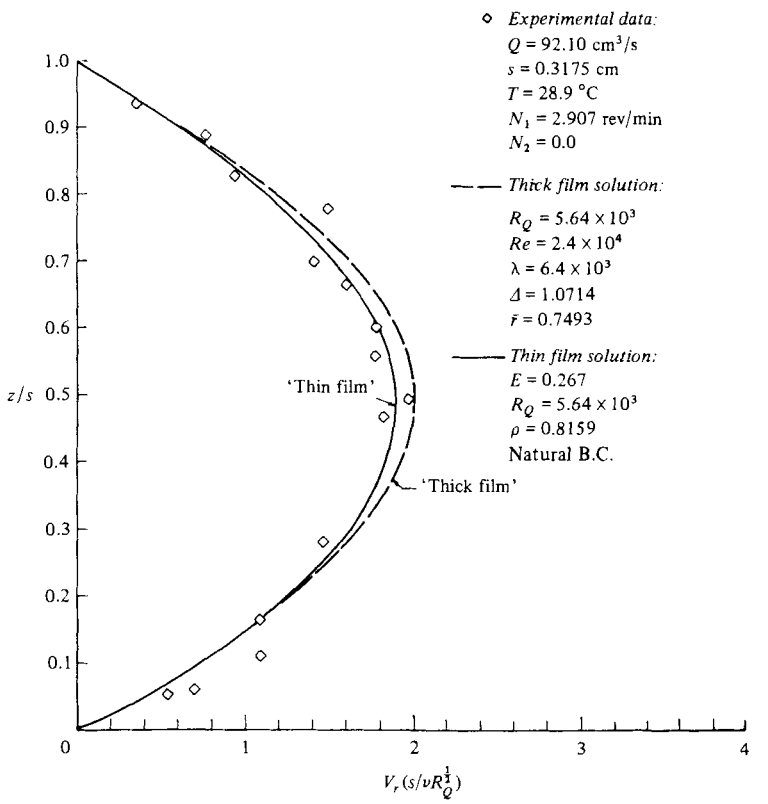

FIGURE 5. Radial velocity, one disk rotating.

$\frac{z}{s}$	$\bar{\bar{V}}_r$		
	$N = 5$	$N = 7$	$N = 9$†
0.2	0.9474	0.9476	0.9472
0.4	1.446	1.446	1.446
0.6	1.452	1.452	1.452
0.8	0.9604	0.9606	0.9604

† Logarithmic distribution of breakpoints.

TABLE 1. Thin-film analysis, perturbation scheme; dimensionless radial velocity at $\rho = 1.0$ ($E = 1.0$, cubic splines)

naturally occurring in the apparatus, devoid of flow straightener devices. Under these conditions small air bubbles, allowed to remain in the system for flow-visualization purposes, were observed to move on a steady circular orbit of radius $\bar{r} \approx 0.35$.

The most probable reason for the poor convergence properties of the present solution in the small-R_Q/Re range is the low dimension of the approximating B-spline subspace. We have not found it possible to go in representation much beyond 52 equations in the set (11*a*, *b*) when calculating the time-dependent problem, due to excessive time requirement on the PDP-10 computer of the University of Pittsburgh.

	$\bar{\bar{V}}_\theta$		
$\frac{z}{s}$	$N = 5$	$N = 7$	$N = 9$†
0.2	0.1239	0.1239	0.1239
0.4	0.2633	0.2634	0.2634
0.6	0.4466	0.4466	0.4466
0.8	0.6951	0.6951	0.6951

† Logarithmic distribution of breakpoints.

TABLE 2. Thin-film analysis, perturbation scheme; dimensionaless tangential velocity at $\rho = 1.0$ ($E = 1.0$, cubic splines)

	$\bar{\bar{V}}_r$		
$\frac{z}{s}$	$N = 5$	$N = 7$	$N = 9$
0.2	0.9540	0.9541	0.9471
0.4	1.436	1.446	1.446
0.6	1.444	1.452	1.453
0.8	0.9660	0.9592	0.9599

TABLE 3. Thin-film analysis, algebraic constraints scheme; dimensionless radial velocity at $\rho = 1.0$ ($E = 1.0$, cubic splines)

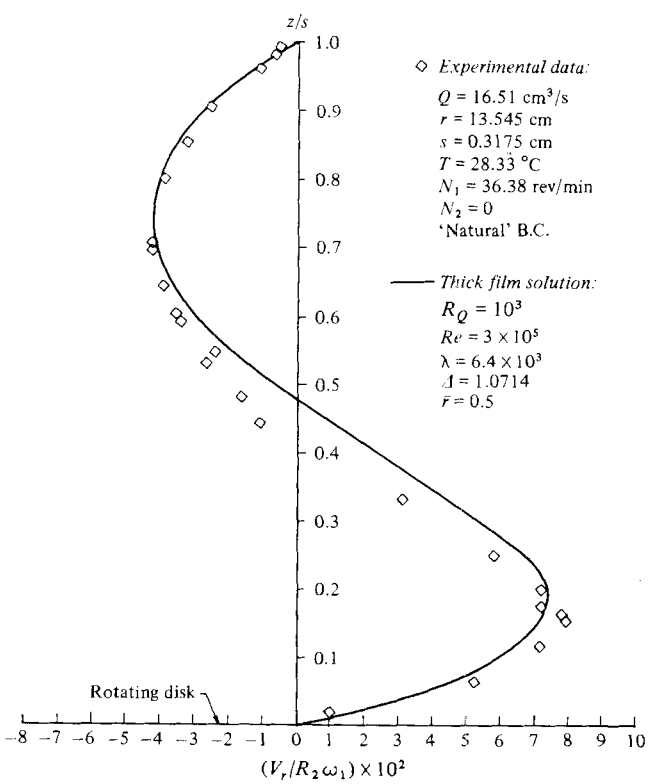

FIGURE 6. Radial velocity, one disk rotating.

	$\bar{\bar{V}}_\theta$		
$\frac{z}{s}$	$N = 5$	$N = 7$	$N = 9$
0.2	0.1213	0.1213	0.1220
0.4	0.2575	0.2579	0.2595
0.6	0.4401	0.4388	0.4405
0.8	0.6865	0.6835	0.6871

TABLE 4. Thin-film analysis, algebraic constraints scheme; dimensionless tangential velocity at $\rho = 1.0$ ($E = 1.0$, cubic splines)

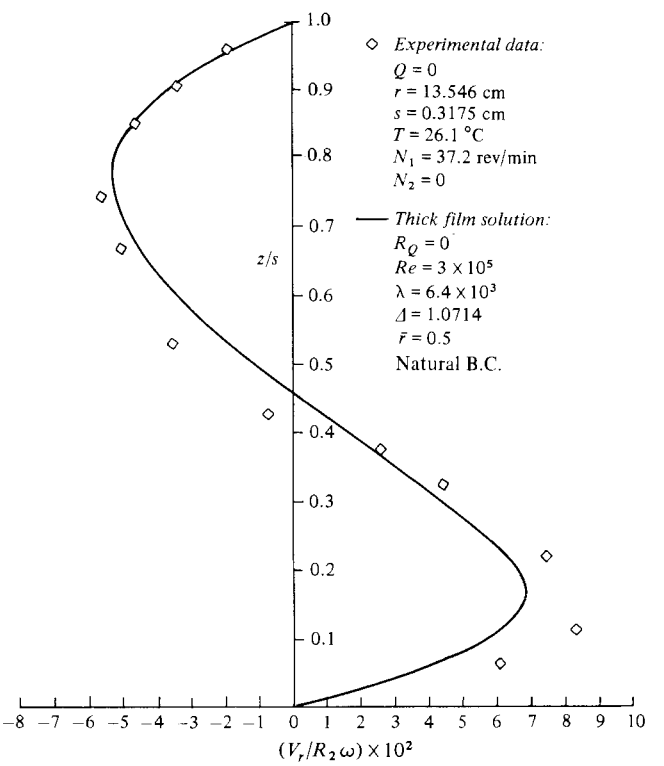

FIGURE 7. Radial velocity, one disk rotating.

Greater resolution is possible, however, if one is content with calculating steady state alone.

Figure 10 is a study in the formation of the toroidal cell. At $Q = 65.08$ cm^3/s the source flow is just large enough to neutralize the return flow of centrifugal effects at $\bar{r} = 0.6$. The local value of the Rossby number is $Ro = 0.0777$. For larger values of Ro than this, convective inertia due to source flow dominates the flow field and radial outflow results. For $Ro < 0.0777$ rotational effects dominate. Under these conditions the thin-film solution shows incipient backflow at $\rho = 0.75$, which translates to a radial position of $\bar{r} = 0.548$. The corresponding value from stationary solution of the full equations is $\bar{r} = 0.6123$, obtained with $N_r = N_z = 8$.

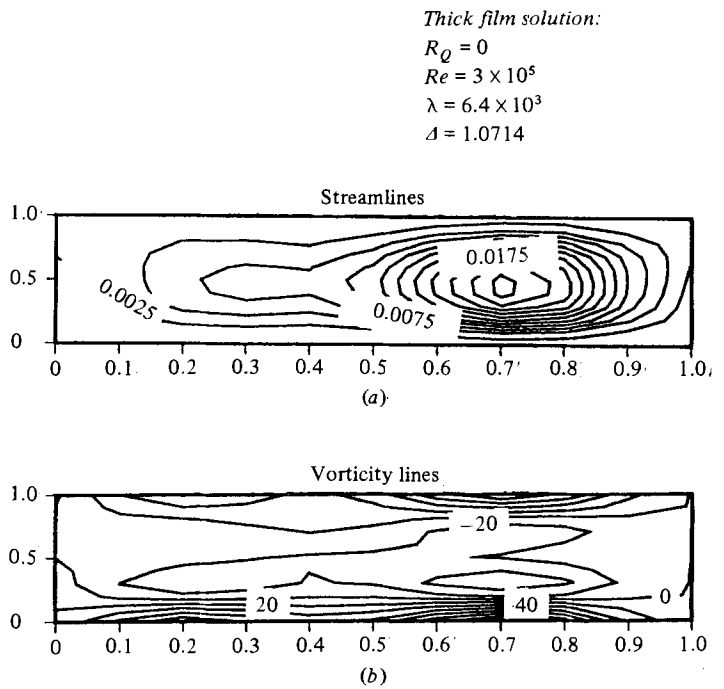

FIGURE 8. Streamlines (*a*) and vorticity lines (*b*).

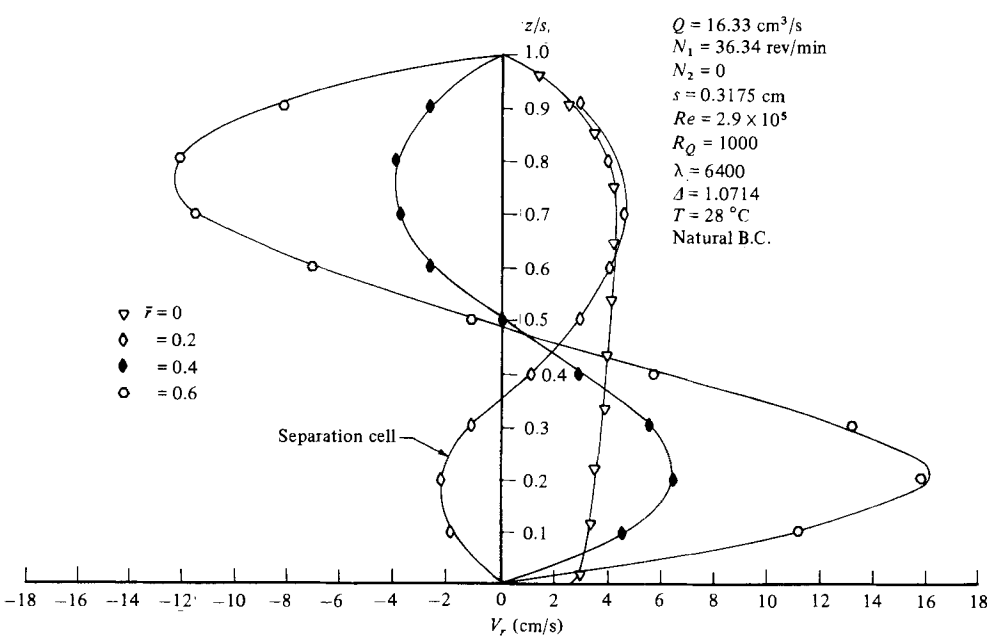

FIGURE 9. Inlet flow lip separation.

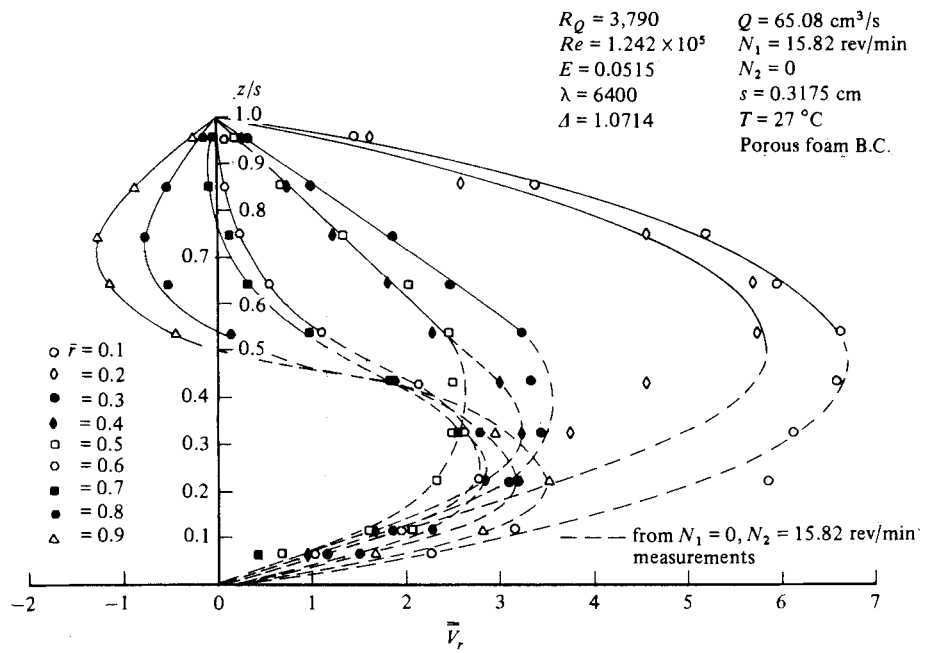

FIGURE 10. Cell development, one disk rotating.

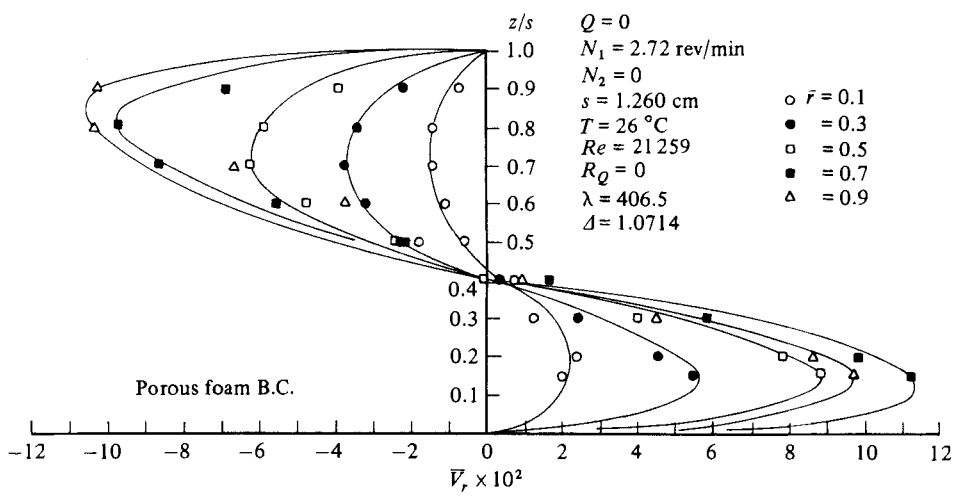

FIGURE 11. Radial velocity.

Figures 11 and 12 show non-dimensional radial and tangential velocities respectively, in an $s = 1.26$ cm channel at $Re = 21259$, when porous foam boundaries are used. The effects of removing the foam (natural boundary conditions) is shown in figures 13 and 14. We note that the radial profiles of figures 11 and 13 are almost identical for $0.3 \leqslant \bar{r} \leqslant 0.5$, i.e. 'far' away from the boundaries located at $\bar{r} = 0$ and $\bar{r} = 1.0$. The tangential velocities, on the other hand, remain similar up to $\bar{r} = 0.5$, as shown in figure 15. This midradius limiting flow is identified with the Batchelor-type flow that is calculated for infinite disks (figure 16). When conditions are such that

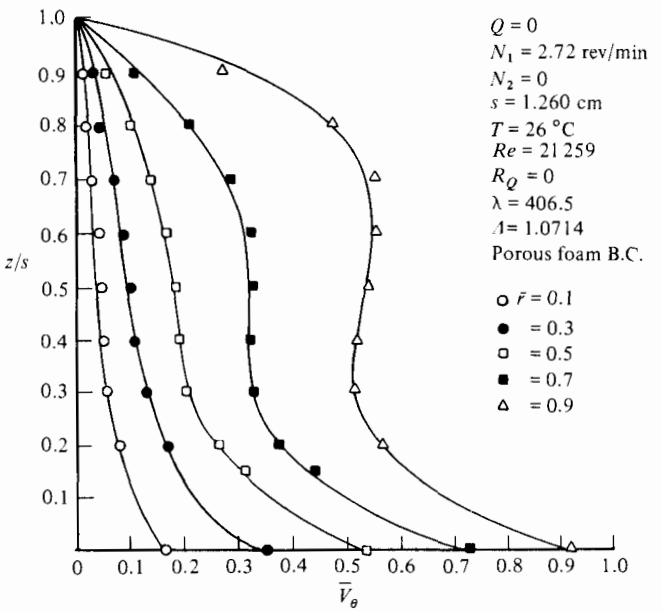

FIGURE 12. Tangential velocity, foam boundaries.

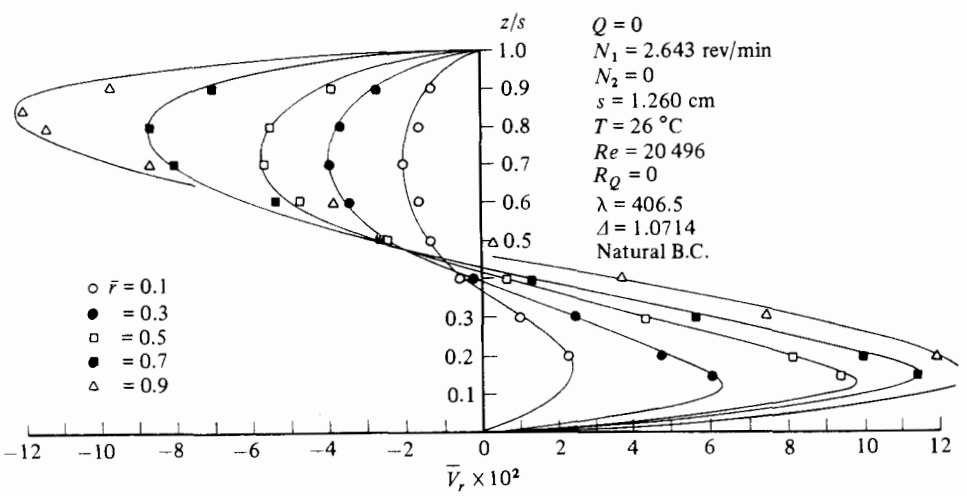

FIGURE 13. Radial velocity.

infinite disk theory predicts multiple solutions, one of the solutions is always of the Batchelor type (Holodniok *et al.* 1977, 1981) and is stable for some region $0 < r/s < (r/s)_c$. The other members of the family of multiple solutions are unstable at all positions, i.e. at all values of the ratio r/s (Szeri *et al.* 1983).

Additional experimental profiles with one disk rotating are shown in figures 17 and 18.

Both the LDV measurements and the calculations reported here are repeatable, irrespective of the starting conditions. We thus conclude that the limiting flow is unique and is independent of flow history.

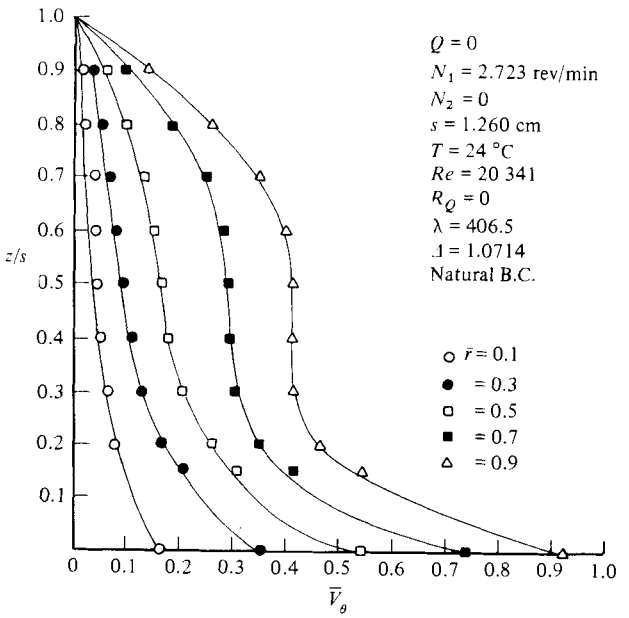

FIGURE 14. Tangential velocity.

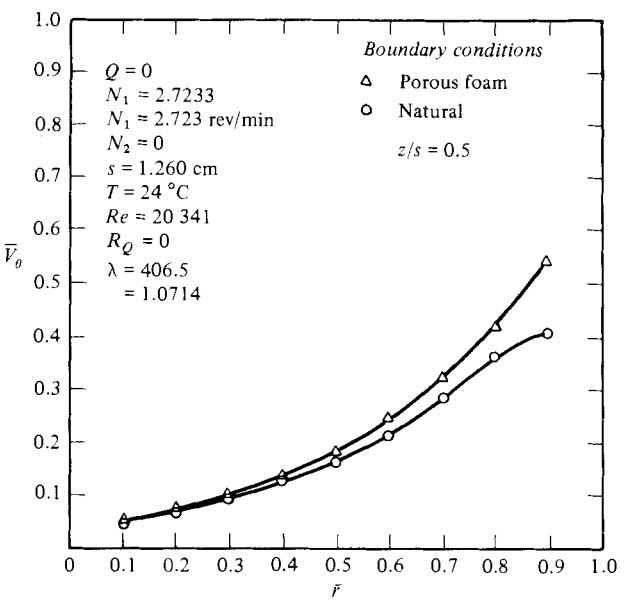

FIGURE 15. Comparison, centreline tangential velocities.

Corotating disks

We have been unable to obtain radial-velocity measurements between corotating disks. If there is a non-zero radial velocity field, it is too small for detection by our LDV system. We are better equipped to measure the large tangential velocities. Our hypothesis is that, if there is significant radial flow, that flow will interact with the tangential motion of the fluid by transporting fluid particles into an alien environment

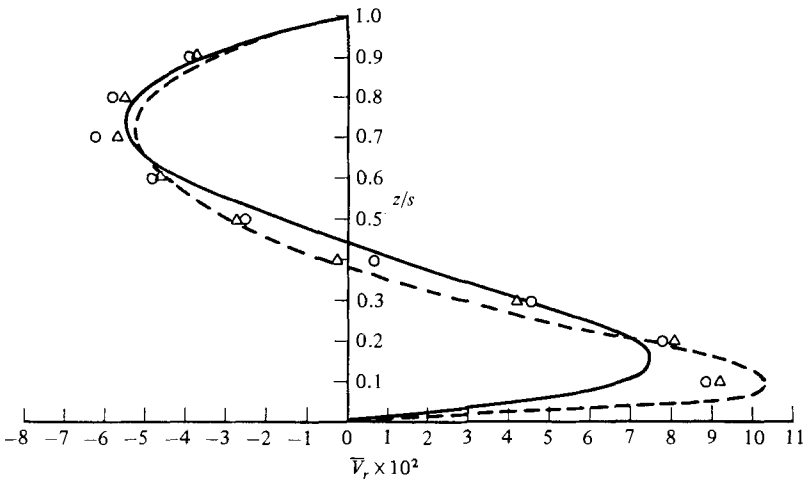

FIGURE 16. Comparison, radial velocities. Experimental: $N_1 = 2.7$ rev/min, $N_2 = 0$, $s = 1.26$ cm, $E^{-1} = 50$: ○, foam boundaries; △, natural boundaries. Theoretical (Lance & Rogers 1961): ——, $E^{-1} = 25$; – – – $E^{-1} = 81$.

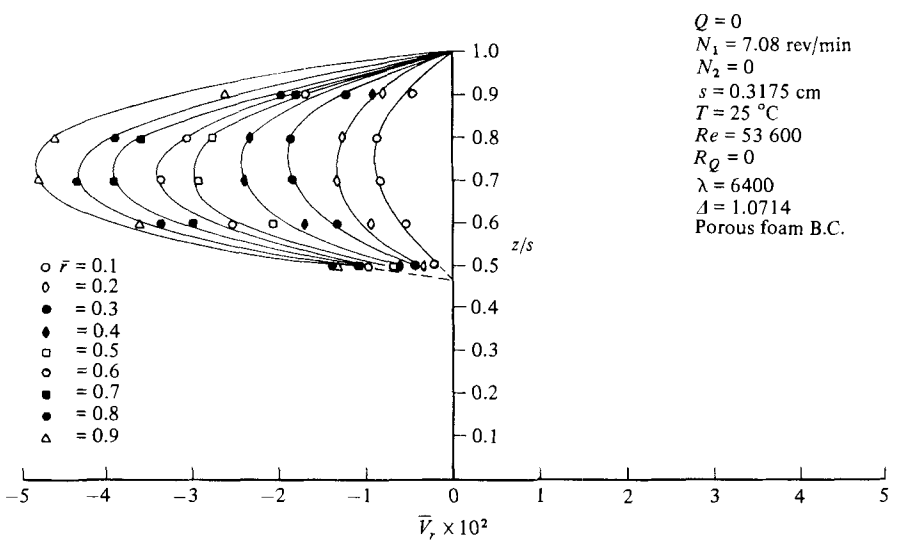

FIGURE 17. Radial velocity.

of angular momentum. If we were to plot dimensionless tangential velocity $\bar{V}_\theta$ against non-dimensional position $\bar{r}$ at zero radial flow, a straight line of slope $1/\Delta$ would result (figure 19). This figure displays experimental data of tangential velocity in dimensionless form, obtained for corotating disks at $Re = 1.94 \times 10^4$. We were unable to detect a difference between the theoretical curve for $\bar{V}_\theta = 0$ and the curve of best fit through experimental points.

Although numerical calculations of corotating disk flows reveal two radially spaced counter-rotating cells, the peak values of the non-dimensional radial velocity are of order 10^{-9} only, as shown in figure 20.

Our conclusion is that, if the motion between corotating disks deviates from rigid body motion, the deviation is slight.

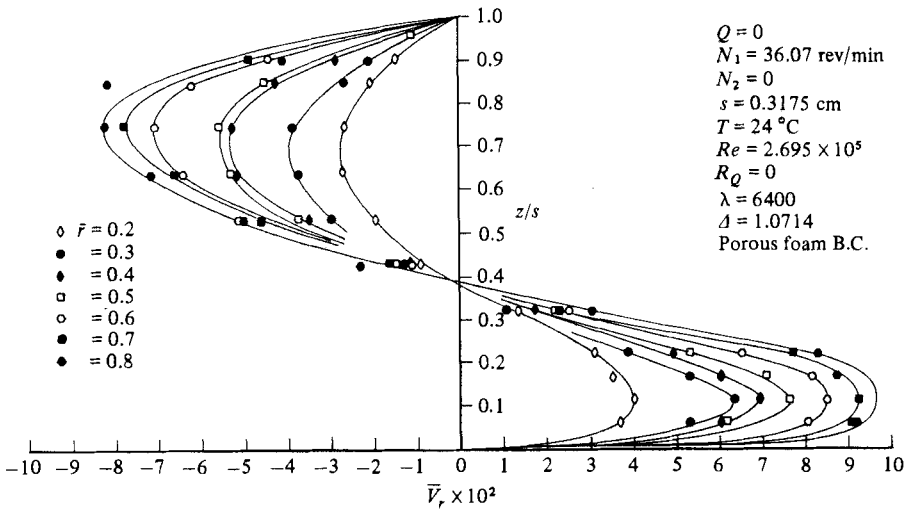

FIGURE 18. Radial velocity.

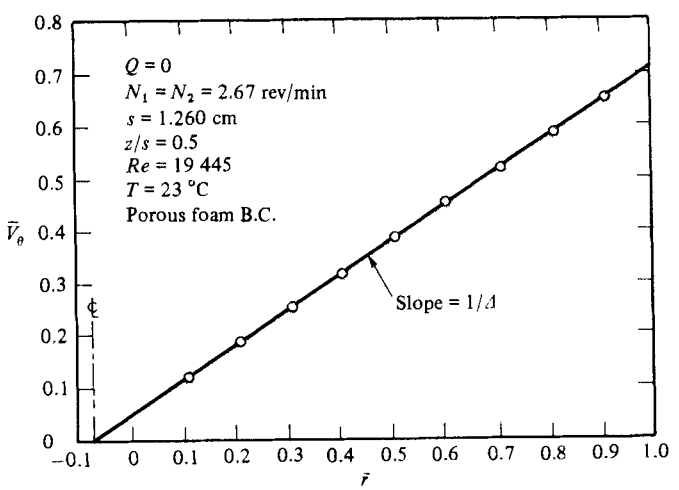

FIGURE 19. Tangential velocity, corotating disks.

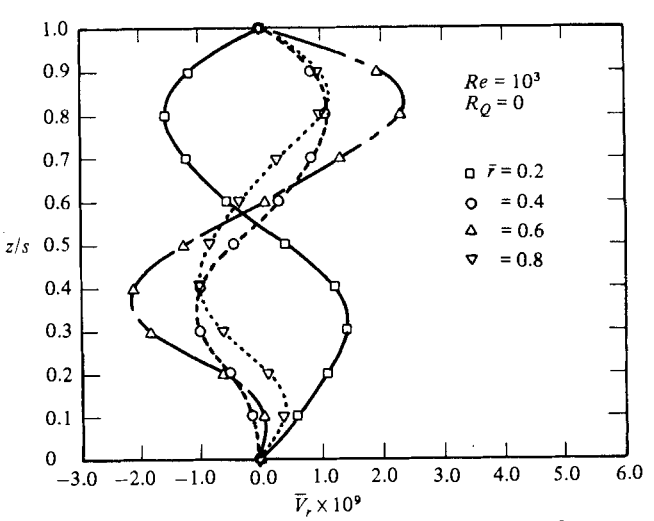

FIGURE 20. Radial velocity, corotating disks.

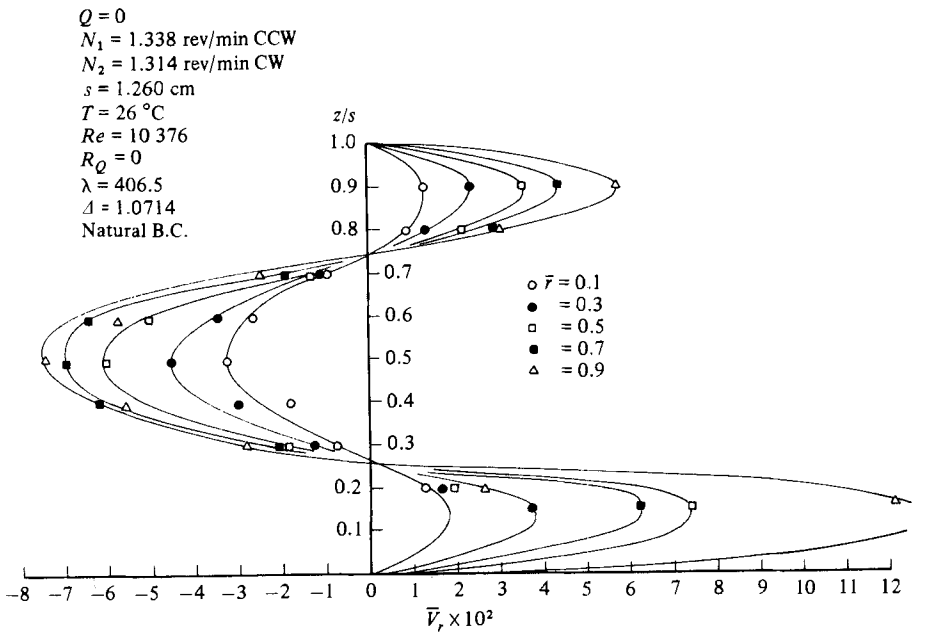

FIGURE 21. Radial velocity.

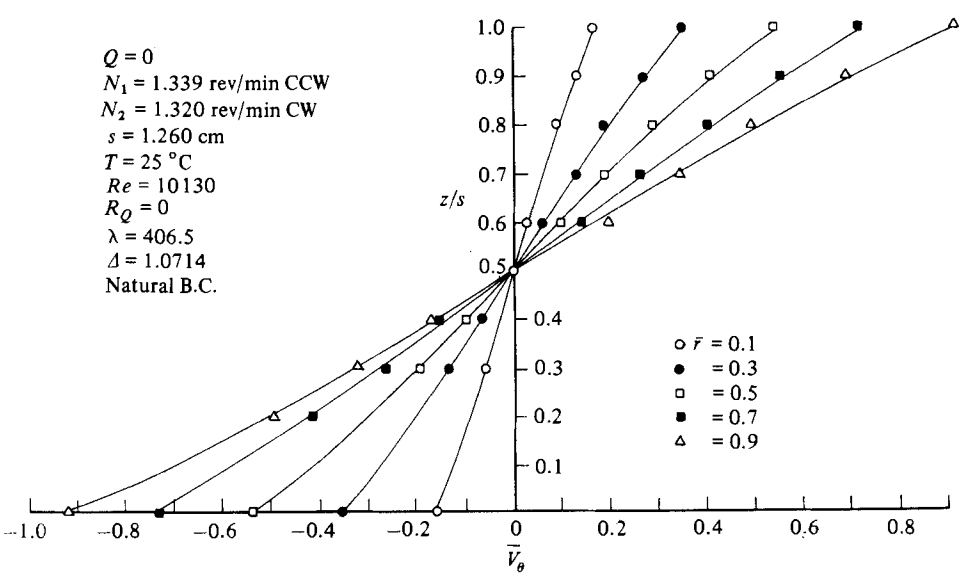

FIGURE 22. Tangential velocity.

Counter-rotating disks

Figures 21 and 22 show the radial and the tangential velocity profiles respectively, at $Re = 10000$ with natural boundary conditions. Figures 23 and 24 show the effect of inserting the foam boundaries. The earlier assertion, that the flow is a limiting flow at midradius, is not obvious when comparing the radial profiles of figures 21 and 23.

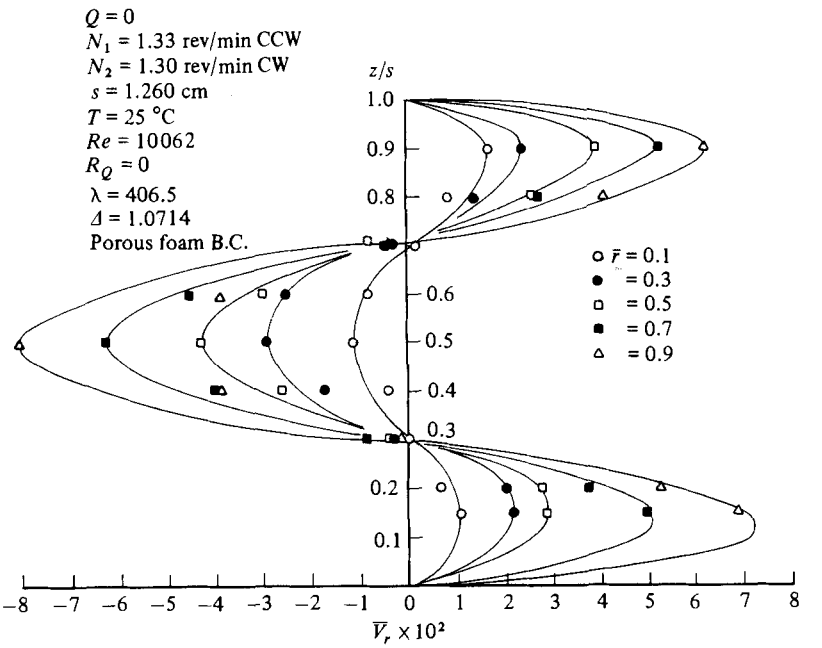

FIGURE 23. Radial velocity.

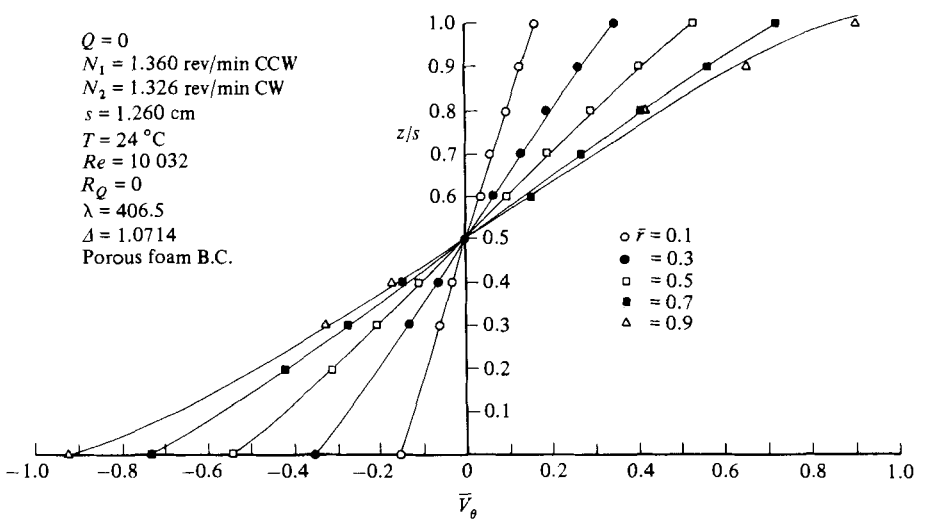

FIGURE 24. Tangential velocity.

The tangential profiles, however, coincide for $r \leqslant 0.7$. This is further demonstrated in figure 25.

Comparison with infinite-disk solutions

It was already shown by Adams & Szeri (1982) that at low Reynolds numbers the mid-channel flow closely resembles the infinite-disk solution of Lance & Rogers (1962). Figures. 26 and 27 display the stationary solutions obtained when the infinite-

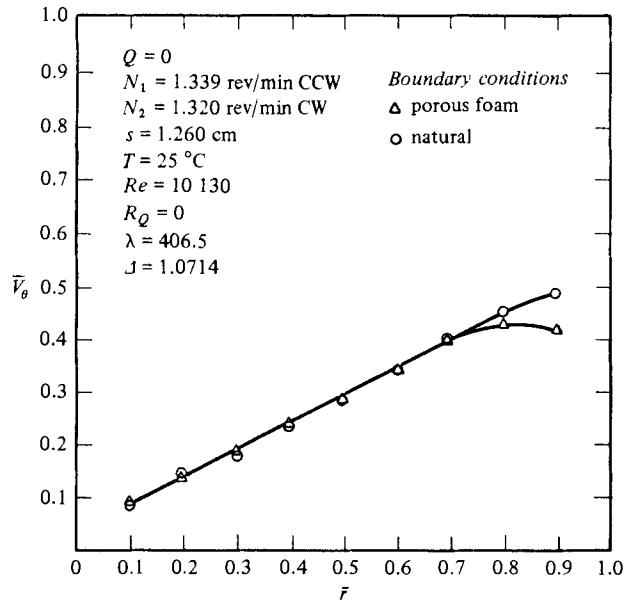

FIGURE 25. Comparison of tangential velocities.

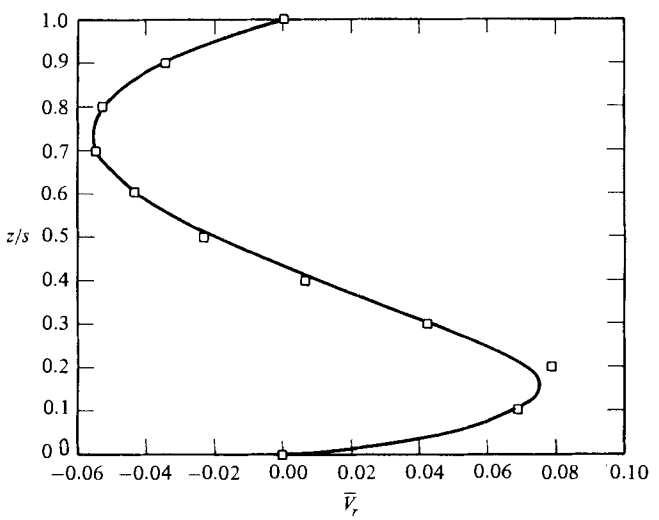

FIGURE 26. Stationary solution, when initial condition is given by infinite-disk profile; radial velocity: □, initial condition $E^{-1} = 25$ (Lance & Rogers 1961); ——; stationary solution $Re = 2500$, $\lambda = 100$.

disk velocity profile of Lance & Rogers is specified as the boundary condition in (7). This initial condition and the stationary solution of the full equations are almost identical, indicating that at least at $Re = 2500$ the infinite-disk solutions satisfy the finite-disk partial differential equations provided that the boundary conditions have been set correctly. And, as was shown in figure 16, the boundary conditions do not have a strong effect on the flow at midradius.

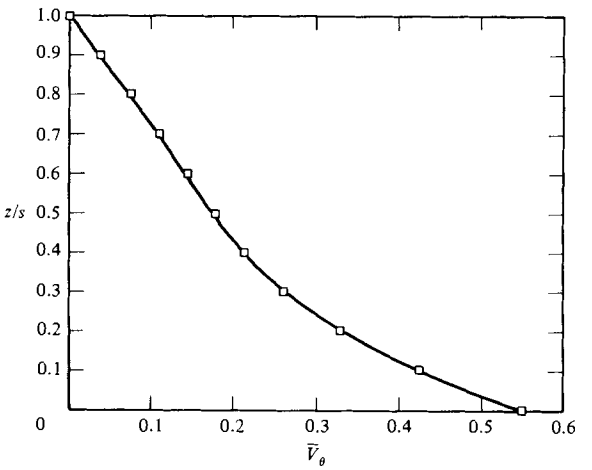

FIGURE 27. Stationary solution, when initial condition is given by infinite-disk profile; tangential velocity: □, initial condition $E^{-1} = 25$ (Lance & Rogers 1961); ——; stationary solution $Re = 2500$, $\lambda = 100$.

This material is based upon work supported by the National Science Foundation under Grant Number MEA 78-21853. This support is gratefully acknowledged. The authors are also indebted to Dr G. Byrne, formerly of the Department of Mathematics and Statistics, University of Pittsburgh, for assistance during the initial stages of computer-software development.

Appendix

Integration over the unit square R yields the Galerkin coefficients

$$\overline{\boldsymbol{Z}}^{(\alpha)}_{ijk} = \int_0^1 B_i^{(a)}(z)\, B_j^{(b)}(z)\, B_k^{(c)}(z)\, \mathrm{d}z,$$

$$\overline{\boldsymbol{z}}^{(\alpha)}_{ij} = \int_0^1 B_i^{(b)}(z)\, B_j^{(c)}(z)\, \mathrm{d}z,$$

$$\overline{\boldsymbol{PK}}^{(\alpha)}_{ijk} = \int_0^1 X^K_{(r)}\, A_i^{(a)}(r)\, A_j^{(b)}(r)\, A_k^{(c)}(r)\, \mathrm{d}r,$$

$$\overline{\boldsymbol{pK}}^{(\alpha)}_{ij} = \int_0^1 X^K_{(r)}\, A_i^{(b)}(r)\, A_j^{(c)}(r)\, \mathrm{d}r,$$

$$\overline{\boldsymbol{NL}}^{(\alpha)}_{ijk} = \int_0^1 X^{-L}(r)\, A_i^{(a)}(r)\, A_j^{(b)}(r)\, A_k^{(c)}(r)\, \mathrm{d}r,$$

$$\overline{\boldsymbol{nL}}^{(\alpha)}_{ij} = \int_0^1 X^{-L}(r)\, A_i^{(b)}(r)\, A_j^{(c)}(r)\, \mathrm{d}r,$$

where

$$a \leqslant b \leqslant c, \quad \alpha = a+b+c+2\ (\text{if } a > 0)+1\ (\text{if } b > 0),\ K \geqslant 0, \quad L > 0.$$

The boundary coefficients in (15) have the following definitions:

$$\overline{\boldsymbol{BC1}}^{(1)}_k = \int_0^1 \phi^{(1)}(z)\, B_k(z)\, \mathrm{d}z - \frac{R_Q}{Re}(\bar{z}^{(0)}_{k,N_z} + \bar{z}^{(0)}_{k,N_z-1})$$

$$\overline{BC1}_k^{(2)} = \int_0^1 \phi_*^{(1)}(z)\, B_k(z)\, \mathrm{d}z,$$

$$\overline{BC1}_m^{(3)} = \int_0^1 \theta^{(1)}(z)\, B_m(z)\, \mathrm{d}z - \frac{\omega_1}{\omega}\bar{z}_{m,1}^{(0)} - \frac{\omega_2}{\omega}\bar{z}_{m,N_z},$$

$$\overline{BC2}_k^{(1)} = \int_0^1 \phi^{(2)}(z)\, B_k(z)\, \mathrm{d}z - \frac{R_q}{Re}(\bar{z}_{k,N_z}^{(0)} + \bar{z}_{k,N_z-1}^{(0)}),$$

$$\overline{BC2}_k^{(2)} = \int_0^1 \phi_*^{(2)}(z)\, B_k(z)\, \mathrm{d}z,$$

$$\overline{BC2}_m^{(3)} = \int_0^1 \theta^{(2)}(z)\, B_m(z)\, \mathrm{d}z - \frac{\omega_1}{\omega}\bar{z}_{m,1}^{(0)} - \frac{\omega_2}{\omega}\bar{z}_{m,N_z}^{(0)}.$$

REFERENCES

ADAMS, M. L. & SZERI, A. Z. 1982 Incompressible flow between finite disks. *Trans. ASME* E: *J. Appl. Mech.* **49**, 1–14.

BATCHELOR, G. K. 1951 Note on a class of solutions of the Navier–Stokes equations representing rotationally symmetric flow. *Q. J. Mech. Appl. Maths* **4**, 29.

DEBOOR, C. 1978 *A Practical Guide to Splines*. Springer.

DIJKSTRA, D. 1980 On the relation between adjacent inviscid cell type solutions to the rotating-disk equations. *J. Engng Maths* **14**, 133–154.

GREGORY, N., STUART, J. T. & WALKER, W. S. 1955 On the stability of three dimensional boundary layers with application to the flow due to a rotating disk. *Phil. Trans. R. Soc. Lond.* **A248**, 155.

HALL, C. A. 1968 On error bounds for spline interpolation. *J. Approx. Theory* **1**, 209–218.

HOLODNIOK, M., KUBICEK, M. & HLAVACEK, V. 1977 Computation of the flow between two rotating coaxial disks. *J. Fluid Mech.* **81**, 680–699.

HOLODNIOK, M., KUBICEK, M. & HLAVACEK, V. 1981 Computation of the flow between two rotating coaxial disks: multiplicity of steady-state solutions. *J. Fluid Mech.* **108**, 227–240.

KÁRMÁN, T. VON 1921 Laminar und turbulente Reibung. *Z. angew. Math. Mech.* **1**, 233.

KREITH, F. 1965 Reverse transition in radial source flow between two parallel plates. *Phys. Fluids* **8**, 1189–1190.

LABBE, F. 1981 Computation of stationary laminar solutions of flow between finite rotating disks. Ph.D. thesis, University of Pittsburgh.

LANCE, G. N. & ROGERS, M. H. 1961 The axially symmetric flow of viscous fluid between two infinite rotating disks. *Proc. R. Soc. Lond.* **A266**, 109–121.

LENTINI, M. & KELLER, H. B. 1980 The von Kármán swirling flows. *SIAM J. Appl. Maths* **38**, 52–63.

MELLOR, G. L., CHAPPLE, P. J. & STOKES, V. K. 1968 On the flow between a rotating and a stationary disk. *J. Fluid Mech.* **31**, 95–112.

NGUYEN, N. D., RIBAULT, J. P. & FLORENT, P. 1975 Multiple solutions for flow between coaxial disks. *J. Fluid Mech.* **68**, 369–388.

ROGERS, M. H. & LANCE, G. N. 1960 The rotationally symmetric flow of a viscous fluid in the presence of an infinite disk. *J. Fluid Mech.* **7**, 617–631.

RUDD, M. J. 1969 A new theoretical model for the laser Doppler-meter. *J. Phys.* E: *Sci. Instr.* **2**, 55–63.

SCHLICHTING, H. 1968 *Boundary Layer Theory*. McGraw-Hill.

SCHNEIDER, S. J. 1982 Flow between finite rotating disks: an experimental study of the basic motion and stability. Ph.D. thesis, University of Pittsburgh.

STEWARTSON, K. 1953 On the flow between two rotating co-axial disks. *Proc. Camb. Phil. Soc.* **3**, 333–341.

SZERI, A. Z. & ADAMS, M. L. 1978 Laminar throughflow between closely spaced rotating disks. *J. Fluid Mech.* **86**, 1–14.

SZERI, A. Z., GIRON, A., SCHNEIDER, S. J. & KAUFMAN, H. N. 1983 Flow between rotating disks. Part 2. Stability. *J. Fluid Mech.* **134**, 133–154.

WEIDMAN, P. D. & REDEKOPP, L. G. 1975 On the motion of a rotating fluid in the presence of an infinite rotating disk. In *Proc. 12th Biennial Fluid Dyn. Symp., Bialowicza, Poland.*

WILSON, L. O. & SCHRYER, N. L. 1978 Flow between a stationary and a rotating disk with suction. *J. Fluid Mech.* **85**, 479–496.

YEH, Y. & CUMMINS, H. Z. 1964 Localized fluid flow measurements with an He–Ne laser spectometer. *Appl. Phys. Lett.* **4**, 176–184.

ZANDBERGEN, P. J. & DIJKSTRA, D. 1977 Non-unique solutions of the Navier–Stokes equations for the Kármán swirling flow. *J. Engng Maths* **11**, 167–188.